



Metal–organic framework supported Au nanoparticles with organosilicone coating for high-efficiency electrocatalytic N₂ reduction to NH₃

Hongming He^a, Qian-Qian Zhu^a, Ying Yan^a, Han-Wen Zhang^a, Zhang-Ye Han^a,
Hongming Sun^a, Jing Chen^a, Cheng-Peng Li^a, Zhihong Zhang^b, Miao Du^{a,b,*}

^a College of Chemistry, Tianjin Key Laboratory of Structure and Performance for Functional Molecules, Tianjin Normal University, Tianjin 300387, China

^b College of Material and Chemical Engineering, Zhengzhou University of Light Industry, Zhengzhou 450001, China

ARTICLE INFO

Keywords:

Ammonia synthesis
Nitrogen reduction reaction
Au@MOF composite
Electrocatalysis
Hydrophobic layer

ABSTRACT

The development of electrocatalysts for nitrogen reduction reaction (NRR) at ambient conditions, with both high NH₃ yield and Faradaic efficiency, is currently a great challenge. To this aim, a unique metal–organic framework (MOF) crystalline matrix with disulfide trimeric unit as the building block was in situ synthesized by integration of dynamic covalent chemistry and coordination chemistry. This MOF with high porosity and excellent stability could be used as a host material to encapsulate well-dispersed Au nanoparticles (NPs) with ultrafine size of 1.9 ± 0.4 nm. After surface modification of Au@MOF by using organosilicone, the hydrophobic-treated Au@MOF (HT Au@MOF) composite shows remarkable electrocatalytic performances for NRR, with the highest NH₃ yield of $49.5 \mu\text{g h}^{-1} \text{mg}_{\text{cat}}^{-1}$ and the state-of-the-art Faradaic efficiency of 60.9% in water medium at ambient conditions. The favorable role of MOFs with functional sulfur groups on modulating the active Au sites and the great effect of hydrophobic coatings on suppressing the competitive hydrogen evolution reaction (HER) have been further demonstrated. This work provides a universal strategy to design composite electrocatalysts for high-efficient and long-term NH₃ production.

1. Introduction

Ammonia is an essential industrial chemical, which is a pre-requisite nutrient for all living creatures and also, a stable hydrogen carrier in the forthcoming field of renewable energy [1]. Although N₂ is extremely abundant and effortlessly available in atmosphere, the conversion of N₂ into NH₃ under ambient conditions is an immensely intractable challenge caused by the strong dipole moment and ultrahigh bond energy ($940.95 \text{ kJ mol}^{-1}$) of the N≡N triple bond [2]. The traditional Haber-Bosch process in industry needs high-purity N₂/H₂ gas and extra harsh conditions [3]. In this context, electrocatalytic nitrogen reduction reaction (NRR) is emerged as a promising approach to artificial N₂ fixation under mild conditions, in which the effective electrocatalysts are most critical [4]. Consequently, various catalysts have been developed for electrocatalytic NRR [5–7], including Fe–N₂ [8], Pt-doped FeP/C [9], Ti₃–x C₂ T_y MXene [10], Pd₃Bi [11], MoS₂ [12], Mo₄P₃ [13] etc. Significantly, gold (Au) is a nice NRR electrocatalyst, because N₂ could be adsorbed on the surface of Au to facilitate the hydrogenation reactions

to produce N₂H_x species ($1 < x < 4$) [14,15]. Recently, some Au-based electrocatalysts, including Au supported on substrates [16] and nano-structured Au (such as hollow nanocages) [17], have been explored for electrosynthesis of NH₃ from N₂. However, either the low NH₃ yield or the poor Faradaic efficiency limits the industrial synthesis of NH₃ by electrocatalytic route, mainly because the serious agglomeration of Au particles leads to low-density catalytic sites [18], and the NRR is normally weakened by competitive hydrogen evolution reaction (HER) [19]. To take full advantage of the expensive Au, one of the most effective approaches is the regulation and reduction of the particle size, because the low-coordination sites on smaller particles will be beneficial to enhance their catalytic activities. Thus, it is of great significance to control the high dispersity of Au sites with boosting catalytic activities and develop the hydrophobic protective coatings to hinder the HER simultaneously.

Recently, metal–organic frameworks (MOFs), as an emerging type of crystalline porous materials prepared by coordination-driven assembly of metal ions or clusters and organic ligands, have received tremendous

* Corresponding author at: College of Chemistry, Tianjin Key Laboratory of Structure and Performance for Functional Molecules, Tianjin Normal University, Tianjin 300387, China.

E-mail address: dumiao@zzuli.edu.cn (M. Du).

<https://doi.org/10.1016/j.apcatb.2021.120840>

Received 25 July 2021; Received in revised form 16 October 2021; Accepted 19 October 2021

Available online 23 October 2021

0926-3373/© 2021 Elsevier B.V. All rights reserved.

attentions owing to their ordered network structures and rich physico-chemical properties [20]. In this context, the thiol (–SH) groups on MOFs can endow them with unique performances for encapsulating Au nanoparticles (NPs), though such MOFs have been underexplored due to the great synthetic challenge [21]. Also, the –SH groups tend to couple to generate disulfide S–S bonds [22], which may act as higher-density sulfur sites for immobilization of Au NPs. Thus, construction of MOFs with disulfide assemblies as the building blocks will be promising to modulate the dispersion of Au NPs, which however has not been achieved so far. Furthermore, dynamic covalent chemistry has drawn interests on the expansion of macrocycles [23], organic cages [24], and pillararenes [25], while few cyclic and caged disulfide architectures have been achieved via self-assembly of sulfhydryl compounds [26]. In fact, discrete disulfide compounds are difficult to control and synthesize due to the facile formation of oligomers or polymers as the by-product [27], and the dispersity and flexibility of disulfide motifs will greatly influence their properties [28]. Inspired by chemosynthesis strategy of disulfide via dynamic covalent chemistry and assembled approach of MOF via coordination chemistry, it is postulated that the thiol-equipped carboxyl compounds may act as the potential building blocks to in situ construct crystalline MOFs with well distributed disulfide motifs (Scheme 1).

To demonstrate the above proof-of-concept, the thiol-equipped dicarboxylic ligand (H_2L), 3,3'-bis(mercapto)biphenyl-*p,p'*-dicarboxylic acid (Fig. S1) [29] was selected to assemble with $Zn(II)$ ions to construct a three-dimensional (3D) MOF. Notably, the caged-shaped disulfide trimer is generated in situ in the resulting MOF, which has not been observed. The high stability and rich disulfide bonds make this MOF as an excellent host matrix to confine the highly dispersed and ultrafine Au NPs. Furthermore, after imparting the surface hydrophobicity onto Au@MOF with organosilicone, the obtained HT Au@MOF composite can integrate both the highly active catalytic sites of Au NPs and hydrophobic MOF shell with nitrogen concentration effect (Scheme 2). As a consequence, the HT Au@MOF composite exhibits outstanding electrocatalytic NRR performances at ambient conditions, with the highest NH_3 yield of $49.5 \mu g h^{-1} mg_{cat}^{-1}$ and the Faradaic efficiency of 60.9% in water.

2. Experimental section

2.1. Materials and methods

All chemical reagents were commercially purchased and used without purification. $^{14}N_2$ gas ($\geq 99.999\%$) and Ar gas ($\geq 99.999\%$)

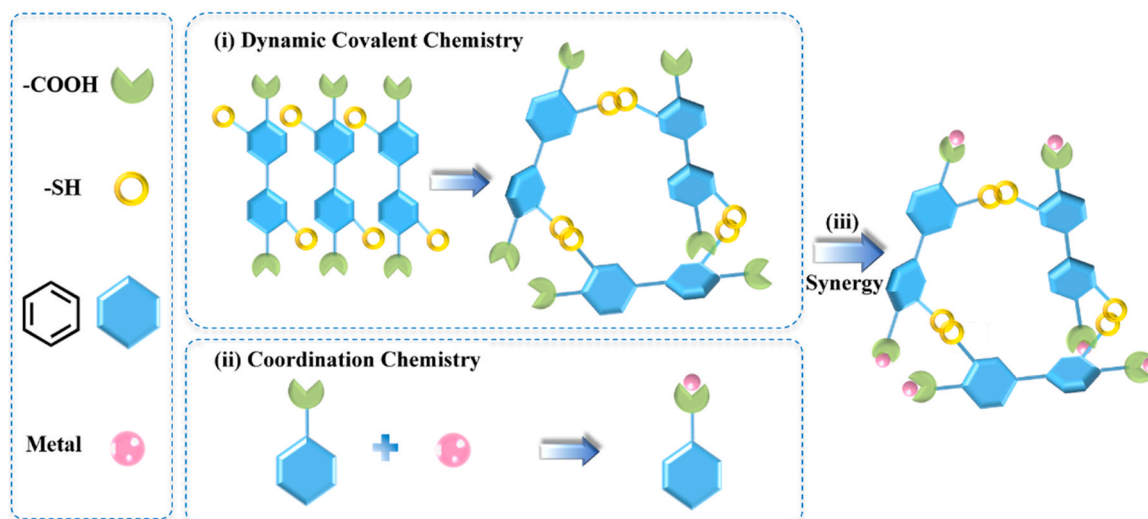
were obtained from Huanyu Co., Ltd. $^{15}N_2$ gas (99%) was purchased from Tianjin Taiya Co., Ltd. Organosilicone (PMX-200–500CS) with the molecular formula of $[-Si(CH_3)_2O-]_n$ (Fig. S2) was acquired from DOWSIL. Powder X-ray diffraction (PXRD) patterns were recorded on a Bruker GADDS diffractometer with Cu-K α ($\lambda = 1.5418 \text{ \AA}$) at 50 kV and 200 mA at ambient temperature. Thermogravimetric analysis (TGA) curves were taken on a Perkin-Elmer thermogravimetric analyzer in 30–800 °C under air flow at a heating rate of $10 \text{ }^\circ\text{C min}^{-1}$. Infrared (IR) spectra were performed on a Bruker ALPHA FT-IR spectrometer in 4000–400 cm^{-1} (with KBr pellets). N_2 adsorption isotherms were taken on a Micromeritics ASAP 2020 surface area analyzer at 77 K. 1H NMR spectra were recorded on a Bruker NMR spectrometer (400 MHz) with the chemical shifts reported as ppm. Inductively coupled plasma optical emission spectrometry (ICP-OES) was conducted on a Thermo Scientific iCAP 6500 model spectrometer. Transmission electron microscopy (TEM) was taken on a Tecnai G² F20 electron microscope. X-ray photoelectron spectroscopy (XPS) was performed on a PHI Quantera SXM spectrometer with monochromatic Mg X-ray radiation source. Electrochemical measurements were taken on a CHI660D electrochemical workstation. Ultraviolet-visible (UV–vis) spectra were measured on a Mapada V-1200 spectrometer.

2.2. Synthesis of MOF

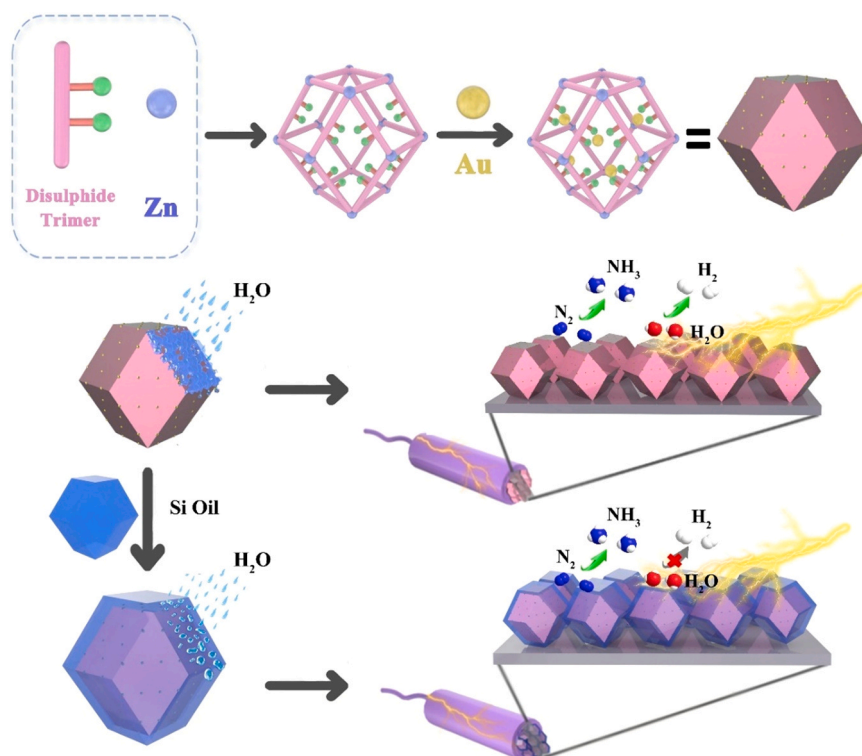
The ligand H_2L was synthesized according to the literature [29]. $Zn(NO_3)_2 \cdot 6H_2O$ (30 mg, 0.1 mmol), H_2L (7 mg, 0.023 mmol), and 1,2,4-triazole (7 mg, 0.1 mmol) were added into a mixed solution of N,N -dimethylformamide (DMF, 1.75 mL), N,N -dimethylacetamide (DMAc, 0.25 mL), water (2.1 mL), and acetonitrile (0.8 mL). After that, 2 M HNO_3 (1.1 mL) was added to the mixture solution, which was putted in an oven at 85 °C for one week. Colorless polygonal crystals were obtained in 62% yield (based on H_2L).

2.3. Synthesis of Au@MOF

In a typical case, a methanol solution (20 mL) of $KAuCl_4$ ($0.1667 mg_{Au} mL^{-1}$) was injected into MOF (100.0 mg) under vacuum. The reaction system was stirred for 2 h in an ice water bath and the phase transfer catalyst tetra-*n*-octylammonium bromide (32.8 mg, 0.06 mmol) was added under continuous N_2 flow for 2 h. After that, a freshly prepared methanol solution of $NaBH_4$ (0.2 M, 5 mL) was added to the mixture dropwise under vigorous stirring. The solution was stirred for 5 h, immediately filtrated and washed with deionized water. The product was dried under vacuum at 80 °C for 12 h to obtain Au@MOF.



Scheme 1. Illustration of the synthetic strategy for MOFs with disulfide motifs.



Scheme 2. Illustration of the electrocatalytic NRR by HT Au@MOF composite.

2.4. Synthesis of HT Au@MOF

Typically, organosilicone (100 mg) was firstly dissolved in n-hexane (15 mL). Au@MOF powders (100 mg) were then immersed in the above organosilicone solution and stirred for 20 min at ambient conditions. The turbid suspension was filtrated and dried in air to achieve HT Au@MOF. The organosilicone coating can be successfully covered over the surface of MOFs by straightforward physical interactions and the high hydrophobicity can ensure the stability of organosilicone on MOFs after exposure to electrolyte. To control the thickness of organosilicone coating over MOFs, different dosages of organosilicone were used in the synthetic route, that is, 50 mg for HT Au@MOF (thin layer) and 150 mg for HT Au@MOF (thick layer).

2.5. Electrochemical NRR measurements

Electrochemical measurements were taken on an electrochemical station by using a three-electrode system, and the two-compartment cell was separated by a Nafion membrane (N117, DuPont). Prior to electrochemical measurements, the Nafion membrane was immersed in 5 wt % H_2O_2 solution at 80°C for 1 h, in deionized water for 0.5 h, and then, in 5 wt% H_2SO_4 water solution for 1 h at 80°C . Subsequently, the used Nafion membrane was obtained after boiling in deionized water for 0.5 h. The glassy carbon electrode was modified by different materials, with SCE and Pt plate ($10 \times 20 \text{ mm}^2$) as the reference and the counter electrodes, respectively. The electrolyte is a water solution of Na_2SO_4 (0.1 M). N_2 and Ar gases were pretreated severally by flowing into 0.1 M KOH and 0.1 M H_2SO_4 water solutions, to ensure no N-containing impurity in the gases for NRR tests [30]. Before each NRR measurement, the electrochemical system was bubbled continuously with N_2 gas for more than 1 h, and the gas was maintained throughout the reactions. Potentiostatic measurements were taken at a series of applied potentials (-0.1 , -0.2 , -0.3 , -0.4 , -0.5 , and -0.6 V) versus RHE for 1 h at ambient temperature. All electrochemical tests were measured at least five times in parallel. The potentials used in this work were converted to RHE using the equation $E(\text{RHE}) = E(\text{SCE}) + 0.0591 \times \text{pH} + 0.242$.

3. Results and discussion

3.1. Crystal structure

Single crystal X-ray diffraction indicates that the as-synthesized MOF

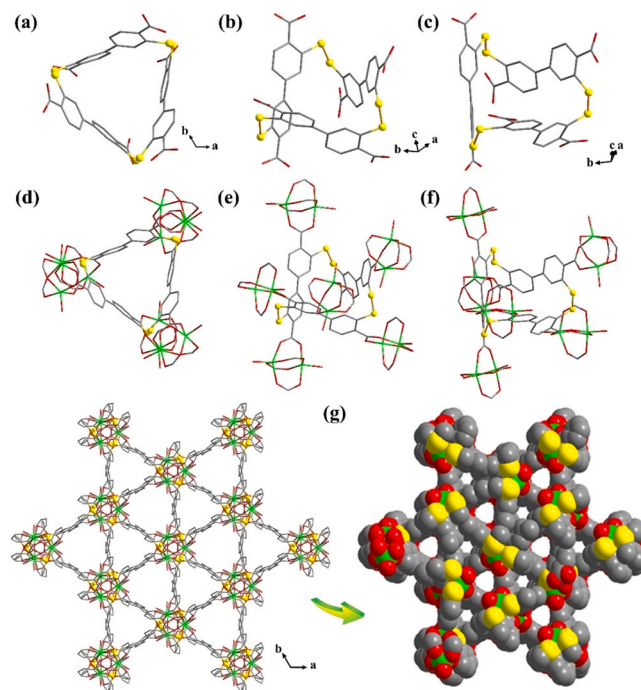


Fig. 1. Crystallographic representation of (a–c) disulphide trimer via dynamic covalent synthesis, (d–f) coordination assembly of disulphide trimers and $[\text{Zn}_2(\text{CH}_3\text{COO})_4]$ clusters, and (g) 3D porous framework with 1D channels (green, Zn; gray, C; red, O; yellow, S).

crystallizes in the $R\bar{3}2$ space group of trigonal system (Table S1). As shown in Fig. 1a–c and Fig. S3, a unique disulfide trimer with available cavity is generated, which contains three S–S bonds and six $-\text{COO}^-$ groups via dynamic covalent synthesis of three sulfhydryl H_2L ligands. In this structure, each disulfide trimeric unit is coordinated to six $[\text{Zn}_2(\text{CH}_3\text{COO})_4]$ paddlewheel motifs (Fig. 1d–f). As a consequence, a 3D porous framework with two types of 1D channels is formed along the crystallographic [001] axis (Fig. 1g and S4). The total void volume after removing the free and coordinated solvents is ca. 42.9% as calculated using the PLATON/VOID routine [31]. A comparison of the IR spectra of H_2L and MOF (Fig. S5) obviously indicates that the $-\text{COOH}$ groups are deprotonated and the $-\text{SH}$ groups are coupled to produce the S–S bonds in MOF. PXRD characterization reveals that the as-synthesized MOF is phase purity, which also shows the excellent stability in air, water, and common organic solvents (Fig. S6).

3.2. Characterizations

The Au@MOF composite was fabricated using a simple impregnation-reduction method. Further, the external surface of MOF was deposited with a hydrophobic organosilicone by the solution-immersion process to obtain the hydrophobic HT Au@MOF composite. PXRD plots of both composites only show the characteristic diffraction peaks of MOF while none obvious signal of Au NPs, indicating the high crystallinity of MOF for loading Au NPs in composites [32]. Moreover, the hydrophobic coating treatment will not affect the MOF framework in HT Au@MOF (Fig. 2a). The Brunauer-Emmett-Teller (BET) surface areas are calculated to 834, 744, and $716 \text{ m}^2 \text{ g}^{-1}$, for the pristine MOF, Au@MOF, and HT Au@MOF, which indicate the successful fabrication

of composites with the lower porosity (Fig. 2b). This result can also be supported by the characteristic peaks of elements in XPS survey spectra for MOF, Au@MOF, and HT Au@MOF (Figs. S7–S9). The high-resolution Au 4f scan for the composite (Fig. 2c) illustrates the spin-orbit doublets at the binding energy of 87.6 eV (Au 4f_{5/2}) and 83.9 eV (Au 4f_{7/2}), which is not found for the pristine MOF (Fig. S10). The XPS spectrum of MOF shows one S 2p signal at 163.3 eV, which shifts to 162.6 eV in Au@MOF, thus indicating the strong interactions between Au and S (Fig. S11) [33,34]. This result evidently illustrates that the S–S group plays a significant role to control the incorporation of Au NPs in Au@MOF. Also, the deconvoluted peaks at the binding energy of 100.4 eV (Si 2p_{1/2}) and 99.8 eV (Si 2p_{3/2}) suggest the existence of organosilicone in HT Au@MOF (Fig. S12). The contact angles were tested to confirm the surface wettability. The water droplet can be quickly absorbed on Au@MOF (Fig. 2d), showing its preferable hydrophilicity. In contrast, the spherical water droplet could freely stand on the surface of HT Au@MOF with a large water contact angle of $154 \pm 0.3^\circ$ (Fig. 2e). These results illustrate that a hydrophobic coating is generated over the external surface of HT Au@MOF to repel the water molecules.

The TEM images clearly indicate the formation of uniform and highly dispersed Au NPs in Au@MOF composite (Figs. S13–S15). The high-resolution TEM (HRTEM) image for HT Au@MOF illustrates the confined Au NPs with an average size of $1.9 \pm 0.4 \text{ nm}$, in which the atomic lattice fringes with the spacing of 0.23 nm agree well with the Au (111) plane (Fig. 3a) [35]. Moreover, the high-angle annular dark field-scanning transmission electron microscopy (HAADF-STEM) and energy-dispersive spectroscopy (EDS) elemental mappings indicate the homogeneous elemental distribution of S, C, O, Zn, and Au in Au@MOF

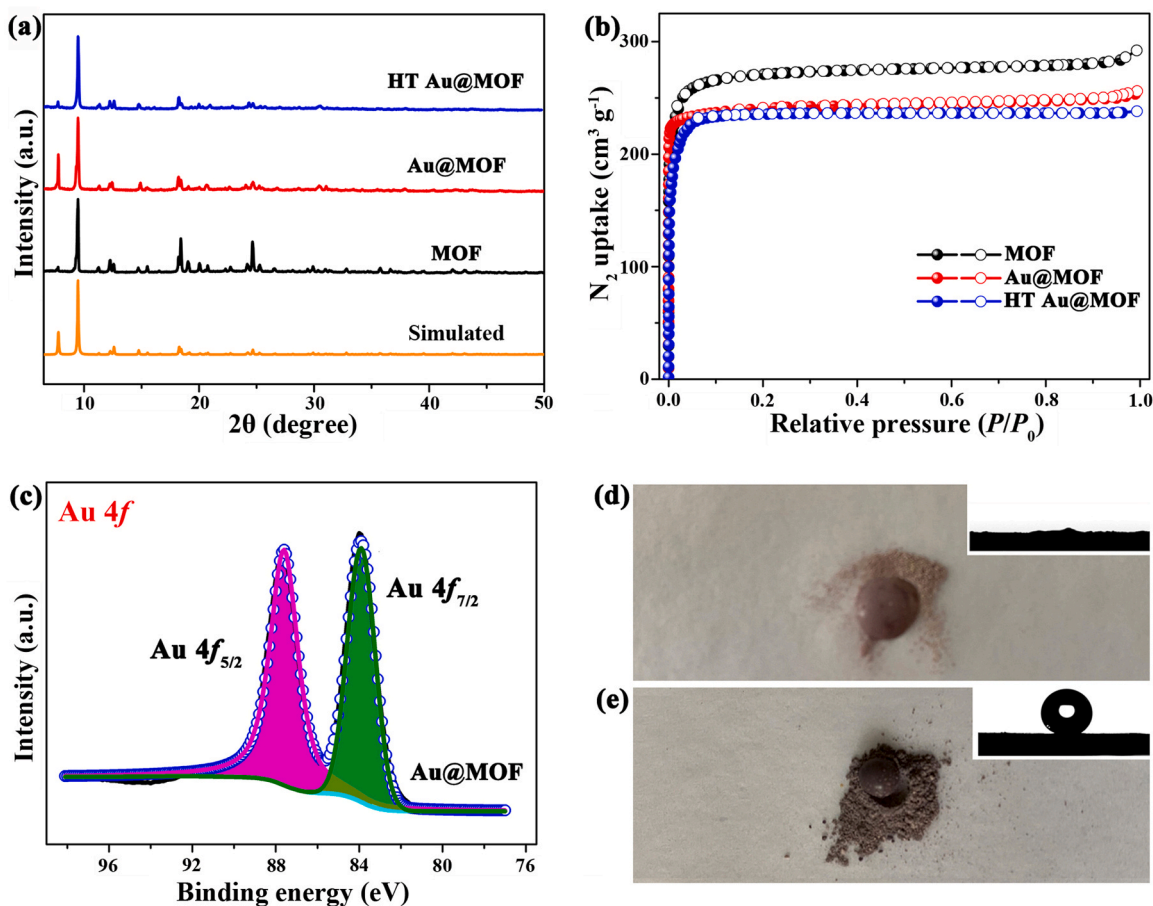


Fig. 2. (a) PXRD patterns and (b) N₂ adsorption/desorption isotherms for MOF, Au@MOF, and HT Au@MOF at 77 K. (c) Au 4f XPS spectrum. Digital photos for (d) Au@MOF and (e) HT Au@MOF samples (inset: contact angle images).

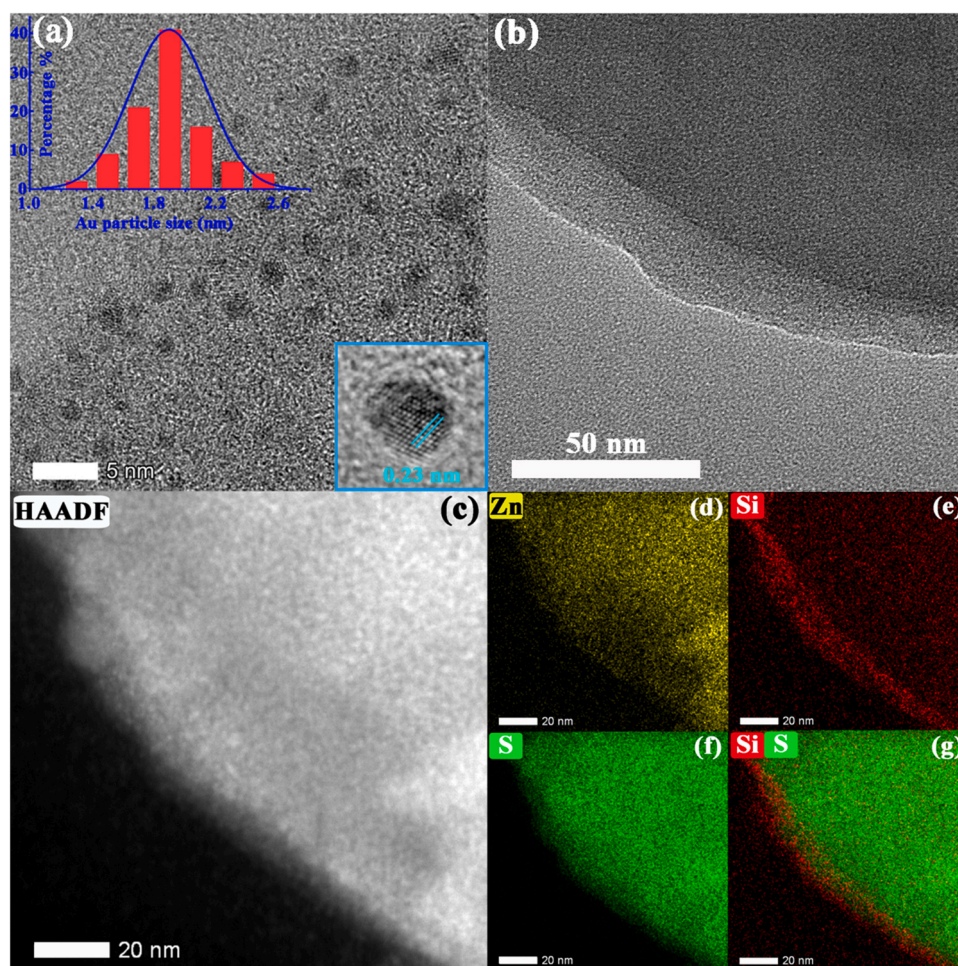


Fig. 3. (a) HRTEM image (inset illustrates the size distribution of Au NPs) for Au@MOF. (b) TEM image, (c) HAADF-STEM image, and EDS mappings of (d) Zn, (e) Si, (f) S, and (g) Si + S for HT Au@MOF.

(Fig. S16). The Au content in Au@MOF is ca. 3.2 wt% as determined by ICP-OES analysis, which is consistent with the residual weight after thermogravimetric experiment (Fig. S17). Also, the existence of organosilicone layer with a thickness of 20 ± 2 nm on Au@MOF can be observed in the TEM image (Fig. 3b). Moreover, the HAADF-STEM image (Fig. 3c) and the EDS mappings (Fig. 3d–g) reveal a homogeneous distribution of Au NPs in the composite and also, a peripheral organosilicone layer on the surface of MOF.

3.3. Electrocatalytic NRR performances

The electrocatalytic activity toward NRR for HT Au@MOF was completely evaluated in a neutral liquid-based electrochemical system at ambient conditions. The yield of NH_3 could be calculated and further confirmed by different approaches, including the spectrophotometric Nessler's reagent method [36], indophenol blue measurement [37], and ^1H NMR spectra [38] with calibration curve (Figs. S18–S21). The linear sweep voltammetry (LSV) plot measured in N_2 -saturated electrolyte shows a significant change at higher current density compared with that in Ar electrolyte due to the occurrence of NRR (Fig. S22). The chronoamperometry (CA) curves at different potentials (Fig. S23) reveal the negligible decay of time-dependent current density in N_2 -saturated environment. Also, the steady current density at different potentials in Na_2SO_4 aqueous solution (0.1 M) manifests the considerable electrocatalytic stability of HT Au@MOF. The Faradaic efficiency and NH_3 production rate can be calculated accurately (see Supplementary Material for details). The strongest absorbance intensity could be

remarkably found at -0.30 V versus reversible hydrogen electrode (RHE) with the highest NH_3 yield, as calculated by the Nessler's reagent method (Fig. 4a). Furthermore, the obvious accumulation of produced NH_3 is observed during the NRR tests (Fig. S24). Remarkably, the highest NH_3 yield of $49.5 \mu\text{g h}^{-1} \text{mg}_{\text{cat}}^{-1}$ could be achieved, also with an excellent Faradaic efficiency of 60.9% (Fig. 4b). Moreover, the reliability of quantitative analysis was confirmed by using the indophenol blue and ^1H NMR approaches, which are all well consistent with the above results (Fig. 4c and Fig. S25). Notably, the NRR performances of HT Au@MOF are superior to other known state-of-the-art electrocatalysts (Fig. 4d and Table S2) [36,39–51]. As a matter of fact, these electrocatalysts suffer from either the poor NH_3 yield or low Faradaic efficiency, which will essentially hinder their applications. The electrochemical active surface area (ECSA) was evaluated by using the double-layer capacitance (C_{dl}), for which HT Au@MOF shows a higher C_{dl} value than the pristine MOF (Fig. S26). Meanwhile, the Nyquist plots demonstrate a lower electron transport resistance of HT Au@MOF than the pristine MOF (Fig. S27). These results reveal that HT Au@MOF could significantly enhance the charge transport to accelerate NRR. Furthermore, none discernable by-product (i.e. hydrazine) was detected at -0.3 V versus RHE using the Watt and Chrisp approach [51] in electrocatalytic NRR process with HT Au@MOF (Figs. S28–S29), revealing the excellent selectivity for NH_3 production (Fig. S30).

In addition, the hydrophobic degree of catalyst surface can be controlled by adjusting the organosilicone layer. When half dosage of organosilicone was used in the synthetic progress of HT Au@MOF, HT Au@MOF (thin layer) bearing a thinner organosilicone layer could be

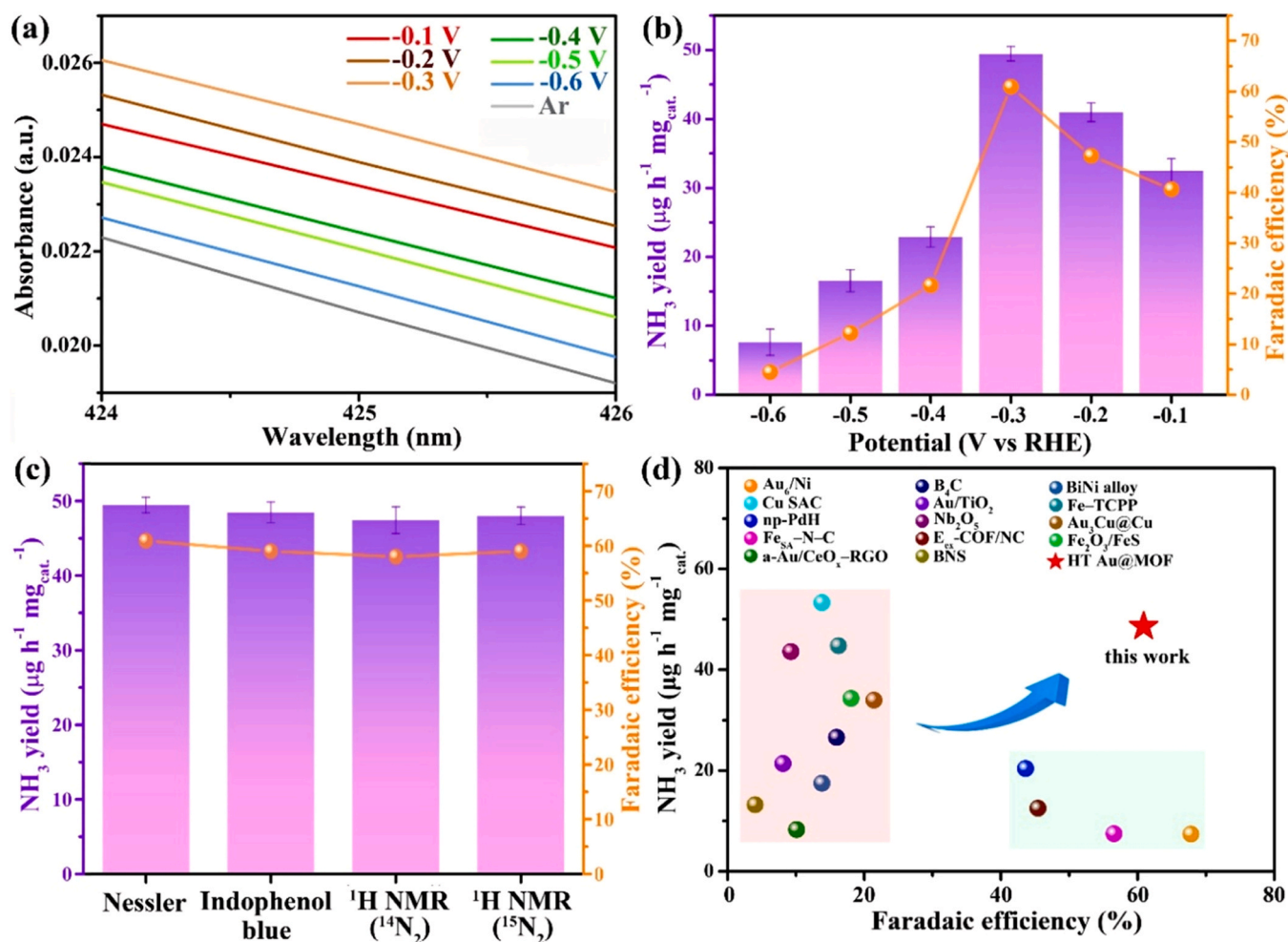


Fig. 4. Electrocatalytic NRR performances of HT Au@MOF. (a) UV-Vis absorption of the electrolytes after electrocatalysis with the spectrophotometric Nessler's reagent method. (b) Ammonia yield and Faradaic efficiency at different potentials. (c) NRR performances at -0.3 V versus RHE by using various approaches. (d) A comparison of NRR performances of NH₃ yield and Faradaic efficiency for HT Au@MOF with other reported materials.

achieved (Fig. S31). Accordingly, HT Au@MOF (thin layer) has a smaller water contact angle of 56.4° (Fig. S32) compared with HT Au@MOF, also with a lower NH₃ yield and Faradaic efficiency (Figs. S33–S34). However, further increasing the dosage of organosilicone will not change the organosilicone layer over HT Au@MOF, indicating the achievement of saturation status. For example, we try to prepare HT Au@MOF (thick layer) by using 1.5-fold dosage of organosilicone. Compared with HT Au@MOF, the as-synthesized HT Au@MOF (thick layer) shows the similar thickness of organosilicone layer (Fig. S35) and water contact angle (Fig. S36) as well as the electrocatalytic NRR performances (Figs. S33–S34). The result reveals that HT Au@MOF is an optimal electrocatalyst for NRR. Notably, both LSV curves of HT Au@MOF (thin layer) and HT Au@MOF (thick layer) exhibit higher current densities in N₂ atmosphere than those in Ar atmosphere due to the occurrence of NRR (Figs. S37–S38). The LSV curves under Ar-saturated environment show that the order of current density is HT Au@MOF (thick layer) ≈ HT Au@MOF > HT Au@MOF (thin layer) > Au@MOF (Fig. S39). This reveals that the organosilicone coating can effectively suppress the HER, thus improving the NRR activity. Similar hydrophobic strategy has also been implemented in CO₂ electroreduction [52,53] and other NRR [13,54] systems. Moreover, no N₂H₄ by-product is observed in the electrolyte after NRR with HT Au@MOF (thin layer) and HT Au@MOF (thick layer) (Figs. S40–S42). Thus, the role of hydrophobic layers on enhancing the NRR performances can be attributed to their inhibiting effect on the HER, with the retainment of high selectivity for NH₃ production.

3.4. Catalytic mechanisms

The control experiments were taken to illustrate the origin of enhanced electrochemical NRR performances for HT Au@MOF composite. As shown in Fig. 5a, the pristine MOF has the negligible electrochemical activity, while the Au NPs with larger size (Fig. S43) present a certain electrocatalytic effect for NRR. Notably, the Au@MOF composite shows a significant electrocatalytic activity, because Au NPs with smaller size can be efficiently loaded in MOF matrix through the affinity between S–S groups and Au NPs. After coating the organosilicone layer onto Au@MOF, the obtained HT Au@MOF composite shows the dramatically boosting electrocatalytic performances. The HT Au@MOF system exhibits 3.5 and 5.9 fold increase of NH₃ yield and Faradaic efficiency, respectively, compared to Au@MOF. The LSV tests under Ar-saturated environment reveal that Au@MOF has an obviously higher current density than that of HT Au@MOF, suggesting the more distinct HER performance for Au@MOF with the absence of organosilicone coatings (Fig. S44). That is to say, the high hydrophobicity for HT Au@MOF considerably suppresses the competitive HER during NRR [13,55]. Moreover, the high porosity of MOF could endow the local saturation and reactants enrichment around the active centers of electrocatalysis to accelerate NRR [56].

To demonstrate the role of disulfide motifs in enhanced NRR activity of HT Au@MOF, three representative MOFs (i.e. DTU-67, 2,5-TP, and Mil-101-SO₃) with different sulfated functional groups (i.e. thiophene or sulfonic group) were synthesized (Figs. S45–S48) [57–59]. Such

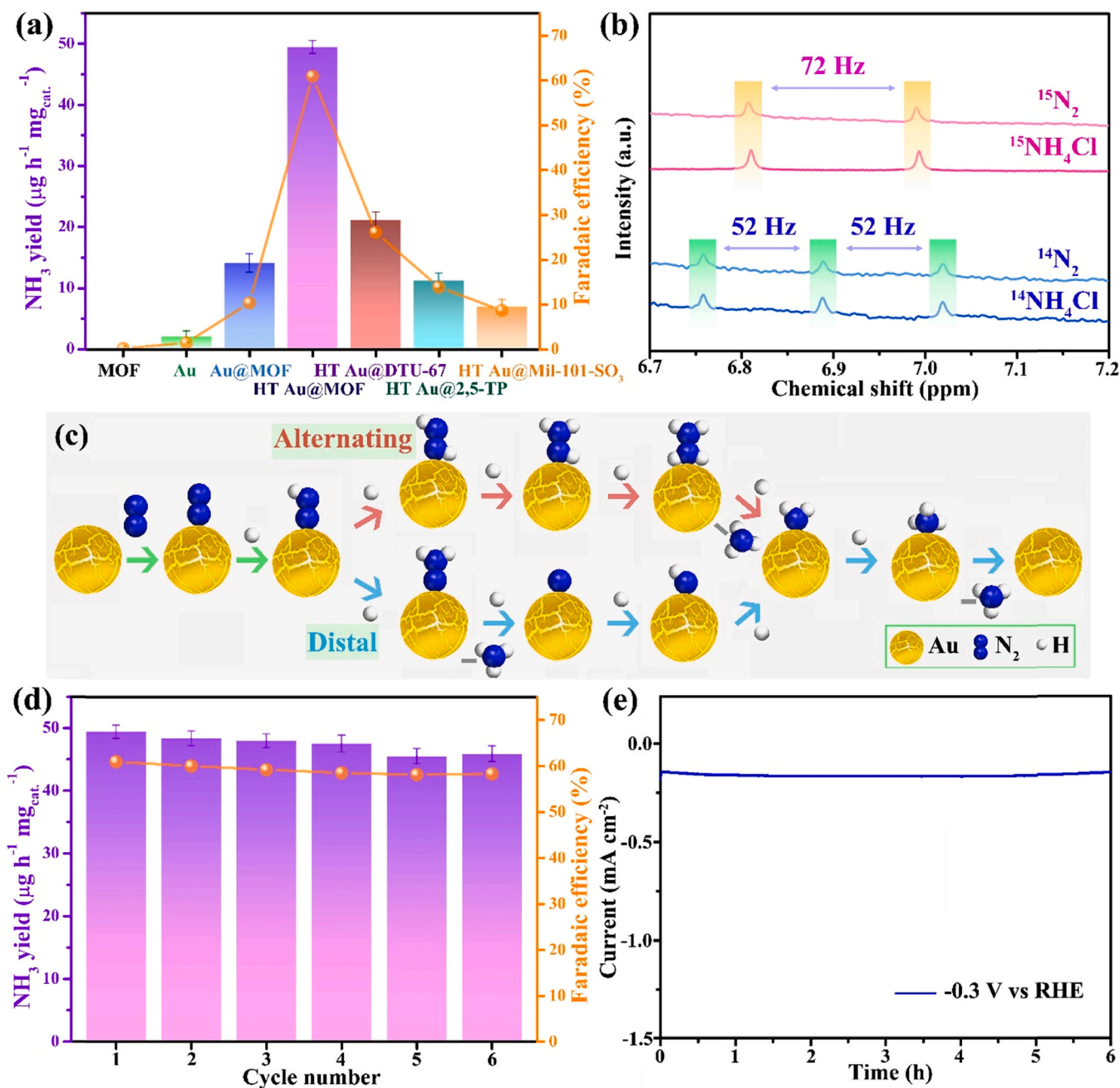


Fig. 5. (a) Comparison of NRR performances by various electrocatalysts. (b) ¹H NMR spectra of ¹⁵N isotope labeling experiments. (c) The proposed pathway for NH₃ formation on Au NPs. (d) Stability and (e) CA curve at -0.3 V versus RHE for HT Au@MOF.

MOFs were similarly employed as the host materials to encapsulate Au NPs and further, coated with organosilicone layer, just as that for HT Au@MOF, to achieve HT Au@DTU-67, HT Au@2,5-TP, and HT Au@Mil-101-SO₃. As expected, these composites exhibit obviously enhanced NRR activity than that of Au NPs, which reveals the universality of this composite strategy of Au sites with MOFs matrixes bearing sulfurated functional groups. Moreover, HT Au@MOF shows the best electrocatalytic performances in the four composite electrocatalysts (Fig. 5a), as evaluated by using the spectrophotometric Nessler's reagent method (Fig. S49), because the Au NPs encapsulated in other three composites are significantly larger than those in HT Au@MOF, thereby reducing their catalytic activities (Figs. S50–S53). As a result, the newly synthesized MOF can act as the most efficient host material for a well dispersion of Au NPs, in which the high-density disulfide is more favorable to the formation of ultrafine Au NPs.

To identify whether nitrogen gas is the sole nitrogen source of produced ammonia during the electrochemical reduction process, the control experiments were subsequently carried out. As described above, the LSV curve (Fig. S22) and UV–vis absorption spectra (Fig. S24) show the electrocatalytic NRR activity of HT Au@MOF in N₂-saturated environment rather than in Ar-saturated electrolyte. This result indicates that the nitrogen source of produced NH₃ should be derived from N₂ gas. Also, the ¹⁵N isotopic labeling experiment was performed to further confirm the nitrogen source of produced NH₃ (Fig. 5b). The ¹H NMR spectroscopy was taken to study the electrolyte using ¹⁴N₂ and ¹⁵N₂ as feeding gases, respectively, for NRR with HT Au@MOF at -0.3 V versus RHE. The standard ¹⁴NH₄Cl and ¹⁵NH₄Cl samples were analyzed as a reference, revealing a triplet for ¹⁴NH₄⁺ and a doublet for ¹⁵NH₄⁺. Notably, the ¹H NMR spectra of the electrolyte after NRR experiment with ¹⁴N₂ atmosphere show the same coupling constant (52 Hz) and

similar signal peaks with those of commercial $^{14}\text{NH}_4\text{Cl}$. As expected, the coupling constant is 72 Hz when using $^{15}\text{N}_2$ as the feeding gas, which is also consistent with that of commercial $^{15}\text{NH}_4\text{Cl}$ [60]. The above results unequivocally illustrate that the produced NH_3 by electrocatalytic NRR completely derive from N_2 gas as the nitrogen source (Figs. S20 and S21).

According to the previous reports on Au NPs-based electrocatalysts for NRR [34,61–63], the possible electrocatalytic NRR mechanism for HT Au@MOF can be described as follows (Fig. 5c). First, the enriched N_2 in MOF can be adsorbed on the confined Au NPs to afford an Au– N_2 bond; second, the H protons in electrolyte could attack the activated N_2 to generate the $\text{N}_2\text{--H}$ bond and weaken the $\text{N}\equiv\text{N}$ triple bond; third, there are two different pathways for NH_3 synthesis, including alternating and distal pathways. For the alternating pathway, the consecutive hydrogenation of $\text{N}_2\text{--H}$ leads to the formation of HNNH , HNNH_2 , and H_2NNH_2 intermediates, which is hydrogenated to release the first NH_3 and further added another H to form the second NH_3 . For the distal pathway, the first NH_3 is released after two successive hydrogenation reactions of $\text{N}_2\text{--H}$, and then the residue N can be added by three H to release the second NH_3 . Since no N_2H_4 is detected in the electrolyte, we tentatively infer that the electrocatalytic NRR mechanism is the distal associative pathway in this case. Moreover, no N_2H_4 is observed during NRR with Au particle or Au@MOF at -0.3 V versus RHE under N_2 atmosphere for 1 h (Fig. S54), which reveals that the reaction pathway will not be influenced by organosilicone layer.

3.5. Stability evaluation

The stability of electrocatalyst is very important for the practical application, which thus was evaluated by six consecutive recycles at -0.3 V versus RHE under N_2 atmosphere for HT Au@MOF. Notably, the Faradaic efficiency and NH_3 yield only exhibit a slight drop (Fig. 5d) in these consecutive electrocatalytic cycles, with almost unchanged CA curve (Fig. 5e), which confirm the favorable stability of HT Au@MOF during the NRR process. The HT Au@MOF composite was also characterized by TEM, XPS, HAADF-STEM and EDS mappings after the NRR experiments, demonstrating that the highly dispersed Au NPs with small sizes still exist in MOF coated with hydrophobic organosilicone (Figs. S55–S59).

4. Conclusion

In summary, the MOF featuring disulfide trimers has been first designed and fabricated by intelligently integrating the dynamic covalent chemistry and coordination chemistry, which can be employed as the host matrix for encapsulating highly dispersed Au NPs to generate the Au@MOF electrocatalyst for NRR. The coating of hydrophobic organosilicone on the surface of Au@MOF can further lead to the greatly enhanced electrocatalytic activity for NRR under ambient conditions. Significantly, the optimized HT Au@MOF electrocatalyst has the highest NH_3 production of $49.5\ \mu\text{g}\ \text{h}^{-1}\ \text{mg}_{\text{cat}}^{-1}$ and a state-of-the-art Faradaic efficiency of 60.9% at -0.3 V versus RHE.

The excellent NRR performances illustrate that the MOFs with defined and rich sulfide sites could serve as good carriers for active Au NPs, which show great superiority to construct high-efficiency catalysts for producing NH_3 from N_2 . Also, the hydrophobic organosilicone is feasible to solve the bottleneck of HER competition during NRR. These approaches allow the facile integration of highly active catalytic sites and hydrophobic porous shell within the same composite. We anticipate that the proposed strategy will provide tremendous opportunities to develop promising electrocatalytic systems for the sustainable NRR and other water-sensitive reactions.

Declaration of Competing Interest

The authors report no declarations of interest.

CRedit authorship contribution statement

Hongming He: Investigation, Methodology, Writing – original draft. **Qian-Qian Zhu:** Investigation, Formal analysis. **Ying Yan:** Investigation, Formal analysis. **Han-Wen Zhang:** Investigation, Formal analysis. **Zhang-Ye Han:** Investigation. **Hongming Sun:** Validation, Formal analysis. **Jing Chen:** Validation, Formal analysis. **Cheng-Peng Li:** Validation, Formal analysis. **Zhihong Zhang:** Validation, Formal analysis. **Miao Du:** Project administration, Writing – review & editing, Supervision.

Acknowledgements

We are grateful to the financial support from the National Natural Science Foundation of China (21571158) and the Key Research Project of University of Henan Province, China (19zx004).

Appendix A. Supporting information

Supplementary data associated with this article can be found in the online version at doi:10.1016/j.apcatb.2021.120840.

References

- [1] J.G. Chen, R.M. Crooks, L.C. Seefeldt, K.L. Bren, R.M. Bullock, M.Y. Darensbourg, P.L. Holland, B. Hoffman, M.J. Janik, A.K. Jones, M.G. Kanatzidis, P. King, K. M. Lancaster, S.V. Lymar, P. Pfromm, W.F. Schneider, R.R. Schrock, Beyond fossil fuel-driven nitrogen transformations, *Science* 360 (2018) eaar6611.
- [2] H. Cheng, L.X. Ding, G.F. Chen, L. Zhang, J. Xue, H. Wang, Molybdenum carbide nanodots enable efficient electrocatalytic nitrogen fixation under ambient conditions, *Adv. Mater.* 30 (2018), 1803694.
- [3] A.J. Martín, T. Shinagawa, J. Pérez-Ramírez, Electrocatalytic reduction of nitrogen: from Haber-Bosch to ammonia artificial leaf, *Chem* 5 (2019) 263–283.
- [4] G. Qing, R. Ghazfar, S.T. Jackowski, F. Habibzadeh, M.M. Ashtiani, C.P. Chen, M. R. Smith, T.W. Hamann, Recent advances and challenges of electrocatalytic N_2 reduction to ammonia, *Chem. Rev.* 120 (2020) 5437–5516.
- [5] S.B. Patil, D.Y. Wang, Exploration and investigation of periodic elements for electrocatalytic nitrogen reduction, *Small* 16 (2020), 2002885.
- [6] H. Liu, L. Wei, F. Liu, Z. Pei, J. Shi, Z.J. Wang, D. He, Y. Chen, Homogeneous, heterogeneous, and biological catalysts for electrochemical N_2 reduction toward NH_3 under ambient conditions, *ACS Catal.* 9 (2019) 5245–5267.
- [7] B. Wu, Y. Lin, X. Wang, L. Chen, Recent advances on electrocatalytic fixation of nitrogen under ambient conditions, *Mater. Chem. Front.* 5 (2021) 5516–5533.
- [8] W. Qiu, N. Yang, D. Luo, J. Wang, L. Zheng, Y. Zhu, E.M. Akinoglu, Q. Huang, L. Shui, R. Wang, G. Zhou, X. Wang, Z. Chen, Precise synthesis of Fe– N_2 with N vacancies coordination for boosting electrochemical artificial N_2 fixation, *Appl. Catal. B-Environ.* 293 (2021), 120216.
- [9] Y. Deng, Z. Xiao, Z. Wang, J. Lai, X. Liu, D. Zhang, Y. Han, S. Li, W. Sun, L. Wang, The rational adjusting of proton-feeding by Pt-doped FeP/C hollow nanorod for promoting nitrogen reduction kinetics, *Appl. Catal. B-Environ.* 291 (2021), 120047.
- [10] Y. Shi, Y. Liu, Vacancy and N dopants facilitated Ti^{3+} sites activity in 3D $\text{Ti}_{3-x}\text{C}_2\text{Ty}$ MXene for electrochemical nitrogen fixation, *Appl. Catal. B-Environ.* 297 (2021), 120482.
- [11] X. Wang, M. Luo, J. Lan, M. Peng, Y. Tan, Nanoporous intermetallic Pd_3Bi for efficient electrochemical nitrogen reduction, *Adv. Mater.* 33 (2021), 2007733.
- [12] J. Chen, C. Zhang, M. Huang, J. Zhang, J. Zhang, H. Liu, G. Wang, R. Wang, The activation of porous atomic layered MoS_2 basal-plane to induce adjacent Mo atom pairs promoting high efficiency electrochemical N_2 fixation, *Appl. Catal. B-Environ.* 285 (2021), 119810.
- [13] L. Xiao, S. Zhu, Y. Liang, Z. Li, S. Wu, S. Luo, C. Chang, Z. Cui, Effects of hydrophobic layer on selective electrochemical nitrogen fixation of self-supporting nanoporous Mo_4P_3 catalyst under ambient conditions, *Appl. Catal. B-Environ.* 286 (2021), 119895.
- [14] Y. Yao, S. Zhu, H. Wang, H. Li, M. Shao, A spectroscopic study on the nitrogen electrochemical reduction reaction on gold and platinum surfaces, *J. Am. Chem. Soc.* 140 (2018) 1496–1501.
- [15] M. Zhang, Z. Wang, H. Yu, S. Wang, Y. Xu, X. Li, L. Wang, H. Wang, A mesoporous Au film with surface sulfur modification for efficient ammonia electrosynthesis, *J. Mater. Chem. A* 8 (2020) 20414–20419.
- [16] J. Zhang, Y. Ji, P. Wang, Q. Shao, Y. Li, X. Huang, Adsorbing and activating N_2 on heterogeneous Au– Fe_3O_4 nanoparticles for N_2 fixation, *Adv. Funct. Mater.* 30 (2020), 1906579.
- [17] M. Nazemi, S.R. Panikkanvalappil, M.A. El-Sayed, Enhancing the rate of electrochemical nitrogen reduction reaction for ammonia synthesis under ambient conditions using hollow gold nanocages, *Nano Energy* 49 (2018) 316–323.
- [18] M.R. Lee, H.K. Lee, Y. Yang, C.S.L. Koh, C.L. Lay, Y.H. Lee, I.Y. Phang, X.Y. Ling, Direct metal writing and precise positioning of gold nanoparticles within

- microfluidic channels for SERS sensing of gaseous analytes, *ACS Appl. Mater. Interfaces* 9 (2017) 39584–39593.
- [19] X. Cui, C. Tang, Q. Zhang, A review of electrocatalytic reduction of dinitrogen to ammonia under ambient conditions, *Adv. Energy Mater.* 8 (2018), 1800369.
 - [20] Y. Cui, B. Li, H. He, W. Zhou, B. Chen, G. Qian, Metal–organic frameworks as platforms for functional materials, *Acc. Chem. Res.* 49 (2016) 483–493.
 - [21] J. He, S. Cheng, Z. Xu, Sulfur chemistry for stable and electroactive metal–organic frameworks: the crosslinking story, *Chem. Eur. J.* 25 (2019) 8654–8662.
 - [22] M.S. Collins, M.E. Carnes, B.P. Nell, L.N. Zakharov, D.W. Johnson, A facile route to old and new cyclophanes via self-assembly and capture, *Nat. Commun.* 7 (2016) 11052.
 - [23] C. Fu, J. Mikšátko, L. Assies, V. Vrkslav, S. Orlandi, M. Kalbáč, P. Kovářček, X. Zeng, B. Zhou, L. Muccioli, D.F. Perepichka, E. Orgiu, Surface-confined macrocyclization via dynamic covalent chemistry, *ACS Nano* 14 (2020) 2956–2965.
 - [24] F. Beuerle, B. Gole, Covalent organic frameworks and cage compounds: design and applications of polymeric and discrete organic scaffolds, *Angew. Chem. Int. Ed.* 57 (2018) 4850–4878.
 - [25] M. Xue, Y. Yang, X. Chi, Z. Zhang, F. Huang, Pillararenes, a new class of macrocycles for supramolecular chemistry, *Acc. Chem. Res.* 45 (2012) 1294–1308.
 - [26] T.A. Shear, F. Lin, L.N. Zakharov, D.W. Johnson, “Design of experiments” as a method to optimize dynamic disulfide assemblies: cages and functionalizable macrocycles, *Angew. Chem. Int. Ed.* 59 (2020) 1496–1500.
 - [27] Y. Lai, X. Kuang, P. Zhu, M. Huang, X. Dong, D. Wang, Colorless, transparent, robust, and fast scratch-self-healing elastomers via a phase-locked dynamic bonds design, *Adv. Mater.* 30 (2018), 1802556.
 - [28] M.S. Collins, N.M. Phan, L.N. Zakharov, D.W. Johnson, Coupling metalloid-directed self-assembly and dynamic covalent systems as a route to large organic cages and cyclophanes, *Inorg. Chem.* 57 (2018) 3486–3496.
 - [29] Y.L. Wong, Y. Diao, J. He, M. Zeller, Z. Xu, A thiol-functionalized UiO-67-type porous single crystal: filling in the synthetic gap, *Inorg. Chem.* 58 (2019) 1462–1468.
 - [30] J. Choi, B.H.R. Suryanto, D. Wang, H.L. Du, R.Y. Hodgetts, F.M.F. Vallana, D. R. MacFarlane, A.N. Simonov, Identification and elimination of false positives in electrochemical nitrogen reduction studies, *Nat. Commun.* 11 (2020) 5546.
 - [31] A.L. Spek, *PLATON*, A Multipurpose Crystallographic Tool, Utrecht University, The Netherlands, 2001.
 - [32] Q. Yang, H.L. Jiang, Oxidation or reduction state of Au stabilized by an MOF: active site identification for the three-component coupling reaction, *Small Methods* 2 (2018), 1800216.
 - [33] Y. Deng, Z. Zhang, P. Du, X. Ning, Y. Wang, D. Zhang, J. Liu, S. Zhang, X. Lu, Embedding ultrasmall Au clusters into the pores of a covalent organic framework for enhanced photostability and photocatalytic performance, *Angew. Chem. Int. Ed.* 59 (2020) 6082–6089.
 - [34] Q.P. Zhang, Y.L. Sun, G. Cheng, Z. Wang, H. Ma, S.Y. Ding, B. Tan, J.H. Bu, C. Zhang, Highly dispersed gold nanoparticles anchoring on post-modified covalent organic framework for catalytic application, *Chem. Eng. J.* 391 (2020), 123471.
 - [35] L. Liu, X. Gu, Y. Cao, X. Yao, L. Zhang, C. Tang, F. Gao, L. Dong, Crystal-plane effects on the catalytic properties of Au/TiO₂, *ACS Catal.* 3 (2013) 2768–2775.
 - [36] Z.H. Xue, S.N. Zhang, Y.X. Lin, H. Su, G.Y. Zhai, J.T. Han, Q.Y. Yu, X.H. Li, M. Antonietti, J.S. Chen, Electrochemical reduction of N₂ into NH₃ by donor-acceptor couples of Ni and Au nanoparticles with a 67.8% Faradaic efficiency, *J. Am. Chem. Soc.* 141 (2019) 14976–14980.
 - [37] J. Wang, L. Yu, L. Hu, G. Chen, H. Xin, X. Feng, Ambient ammonia synthesis via palladium-catalyzed electrohydrogenation of dinitrogen at low overpotential, *Nat. Commun.* 9 (2018) 1795.
 - [38] A.C. Nielander, J.M. McEnaney, J.A. Schwalbe, J.G. Baker, S.J. Blair, L. Wang, J. G. Pelton, S.Z. Andersen, K. Enemark-Rasmussen, V. Čolić, S. Yang, S.F. Bent, M. Carnegello, J. Kibsgaard, P.C.K. Vesborg, I. Chorkendorff, T.F. Jaramillo, A versatile method for ammonia detection in a range of relevant electrolytes via direct nuclear magnetic resonance techniques, *ACS Catal.* 9 (2019) 5797–5802.
 - [39] W. Zang, T. Yang, H. Zou, S. Xi, H. Zhang, X. Liu, Z. Lou, Y. Du, Y.P. Feng, L. Shen, L. Duan, J. Wang, S.J. Pennycook, Copper single atoms anchored in porous nitrogen-doped carbon as efficient pH-universal catalysts for the nitrogen reduction reaction, *ACS Catal.* 9 (2019) 10166–10173.
 - [40] M. Wang, S. Liu, T. Qian, J. Liu, J. Zhou, H. Ji, J. Xiong, J. Zhong, C. Yan, Over 56.55% Faradaic efficiency of ambient ammonia synthesis enabled by positively shifting the reaction potential, *Nat. Commun.* 10 (2019) 341.
 - [41] W. Qiu, X.Y. Xie, J. Qiu, W.H. Fang, R. Liang, X. Ren, X. Ji, G. Cui, A.M. Asiri, G. Cui, B. Tang, X. Sun, High-performance artificial nitrogen fixation at ambient conditions using a metal-free electrocatalyst, *Nat. Commun.* 9 (2018) 3485.
 - [42] M.M. Shi, D. Bao, B.R. Wulan, Y.H. Li, Y.F. Zhang, J.M. Yan, Q. Jiang, Au sub-nanoclusters on TiO₂ toward highly efficient and selective electrocatalyst for N₂ conversion to NH₃ at ambient conditions, *Adv. Mater.* 29 (2017), 1606550.
 - [43] S.J. Li, D. Bao, M.M. Shi, B.R. Wulan, Y.M. Yan, Q. Jiang, Amorphizing of Au nanoparticles by CeO_x-RGO hybrid support towards highly efficient electrocatalyst for N₂ reduction under ambient conditions, *Adv. Mater.* 29 (2017), 1700001.
 - [44] J. Han, Z. Liu, Y. Ma, G. Cui, F. Xie, F. Wang, Y. Wu, S. Gao, Y. Xu, X. Sun, Ambient N₂ fixation to NH₃ at ambient conditions: using Nb₂O₅ nanofiber as a high-performance electrocatalyst, *Nano Energy* 52 (2018) 264–270.
 - [45] S. Liu, M. Wang, T. Qian, H. Ji, J. Liu, C. Yan, Facilitating nitrogen accessibility to boron-rich covalent organic frameworks via electrochemical excitation for efficient nitrogen fixation, *Nat. Commun.* 10 (2019) 3898.
 - [46] X. Zhang, T. Wu, H. Wang, R. Zhao, H. Chen, T. Wang, P. Wei, Y. Luo, Y. Zhang, X. Sun, Boron nanosheet: an elemental two-dimensional (2D) material for ambient electrocatalytic N₂-to-NH₃ fixation in neutral media, *ACS Catal.* 9 (2019) 4609–4615.
 - [47] Z. Fang, P. Wu, Y. Qian, G. Yu, Gel-derived amorphous bismuth–nickel alloy promotes electrocatalytic nitrogen fixation via optimizing nitrogen adsorption and activation, *Angew. Chem. Int. Ed.* 60 (2021) 4275–4281.
 - [48] M. Cong, X. Chen, K. Xia, X. Ding, L. Zhang, Y. Jin, Y. Gao, L. Zhang, Selective nitrogen reduction to ammonia on iron porphyrin-based single-site metal–organic frameworks, *J. Mater. Chem. A* 9 (2021) 4673–4678.
 - [49] S. Liu, Y. Xu, S. Jiao, W. Tian, T. Zhou, Z. Wang, X. Li, L. Wang, H. Wang, Rational construction of Au₃Cu/Cu nanocages with porous core–shell heterostructured walls for enhanced electrocatalytic N₂ fixation, *J. Mater. Chem. A* 9 (2021) 8372–8377.
 - [50] T. Chen, H. Ying, C. Zhang, J. Bi, Z. Li, J. Hao, Engineering an Fe₂O₃/FeS hybrid catalyst from a deep eutectic solvent for highly efficient electrocatalytic N₂ fixation, *Chem. Commun.* 57 (2021) 6688–6691.
 - [51] W. Xu, G. Fan, J. Chen, J. Li, L. Zhang, S. Zhu, X. Su, F. Cheng, J. Chen, Nanoporous palladium hydride for electrocatalytic N₂ reduction under ambient conditions, *Angew. Chem. Int. Ed.* 59 (2020) 3511–3516.
 - [52] P. Yue, Q. Fu, J. Li, L. Zhang, L. Xing, Z. Kang, Q. Liao, X. Zhu, Triple-phase electrocatalysis for the enhanced CO₂ reduction to HCOOH on a hydrophobic surface, *Chem. Eng. J.* 405 (2021), 126975.
 - [53] K. Lv, C. Teng, M. Shi, Y. Yuan, Y. Zhu, J. Wang, Z. Kong, X. Lu, Y. Zhu, Hydrophobic and electronic properties of the E-MoS₂ nanosheets induced by FAS for the CO₂ electroreduction to syngas with a wide range of CO/H₂ ratios, *Adv. Funct. Mater.* 28 (2018), 1802339.
 - [54] Z. Du, J. Liang, S. Li, Z. Xu, T. Li, Q. Liu, Y. Luo, F. Zhang, Y. Liu, Q. Kong, X. Shi, B. Tang, A.M. Asiri, B. Li, X. Sun, Alkylthiol surface engineering: an effective strategy toward enhanced electrocatalytic N₂-to-NH₃ fixation by a CoP nanoarray, *J. Mater. Chem. A* 9 (2021) 13861–13866.
 - [55] Y. Ren, C. Yu, X. Tan, H. Huang, Q. Wei, J. Qiu, Strategies to suppress hydrogen evolution for highly selective electrocatalytic nitrogen reduction: challenges and perspectives, *Energy Environ. Sci.* 14 (2021) 1176–1193.
 - [56] Y. Yang, S.Q. Wang, H. Wen, T. Ye, J. Chen, C.P. Li, M. Du, Nanoporous gold embedded ZIF composite for enhanced electrochemical nitrogen fixation, *Angew. Chem. Int. Ed.* 58 (2019) 15362–15366.
 - [57] C. Hu, W. Xu, H. Li, S. Zhou, X. Mo, P. Zhang, K. Tang, Highly efficient adsorption of Au(III) from water by a novel metal–organic framework constructed with sulfur-containing ligands and Zn(II), *Ind. Eng. Chem. Res.* 58 (2019) 17972–17979.
 - [58] H. Furukawa, F. Gándara, Y.B. Zhang, J. Jiang, W.L. Queen, M.R. Hudson, O. M. Yaghi, Water adsorption in porous metal–organic frameworks and related materials, *J. Am. Chem. Soc.* 136 (2014) 4369–4381.
 - [59] D.T. Genna, L.Y. Pfund, D.C. Samblanet, A.G. Wong-Foy, A.J. Matzger, M. S. Sanford, Rhodium hydrogenation catalysts supported in metal organic frameworks: influence of the framework on catalytic activity and selectivity, *ACS Catal.* 6 (2016) 3569–3574.
 - [60] J. Wang, B. Huang, Y. Ji, M. Sun, T. Wu, R. Yin, X. Zhu, Y. Li, Q. Shao, X. Huang, A general strategy to glassy M–Te (M = Ru, Rh, Ir) porous nanorods for efficient electrochemical N₂ fixation, *Adv. Mater.* 32 (2020), 1907112.
 - [61] Y. Wan, J. Xu, R. Lv, Heterogeneous electrocatalysts design for nitrogen reduction reaction under ambient conditions, *Mater. Today* 27 (2019) 69–90.
 - [62] J. Rittle, J.C. Peters, An Fe–N₂ complex that generates hydrazine and ammonia via Fe=NNH₂: demonstrating a hybrid distal-to-alternating pathway for N₂ reduction, *J. Am. Chem. Soc.* 138 (2016) 4243–4248.
 - [63] H. Wang, H. Yu, Z. Wang, Y. Li, Y. Xu, X. Li, H. Xue, L. Wang, Electrochemical fabrication of porous Au film on Ni foam for nitrogen reduction to ammonia, *Small* 15 (2019), 1804769.